



Aberration-corrected three-dimensional positioning with a single-shot metalens array

WENWEI LIU,^{1,†} DINA MA,^{1,†} ZHANCHENG LI,¹ HUA CHENG,^{1,5} DUK-YONG CHOI,² JIANGUO TIAN,¹ AND SHUQI CHEN^{1,3,4,*}

¹The Key Laboratory of Weak Light Nonlinear Photonics, Ministry of Education, School of Physics and TEDA Institute of Applied Physics, Nankai University, Tianjin 300071, China

²Laser Physics Centre, Research School of Physics, Australian National University, Canberra, ACT 2601, Australia

³The Collaborative Innovation Center of Extreme Optics, Shanxi University, Taiyuan, Shanxi 030006, China

⁴Collaborative Innovation Center of Light Manipulations and Applications, Shandong Normal University, Jinan 250358, China

⁵e-mail: hcheng@nankai.edu.cn

*Corresponding author: schen@nankai.edu.cn

Received 24 August 2020; revised 20 October 2020; accepted 28 October 2020 (Doc. ID 406039); published 3 December 2020

Three-dimensional (3D) positioning with the correction of imaging aberrations in the photonic platform remains challenging. Here, we combine techniques from nanophotonics and machine vision to significantly improve the imaging and positioning performance. We use a titanium dioxide metalens array operating in the visible region to realize multipole imaging and introduce a cross-correlation-based gradient descent algorithm to analyze the intensity distribution in the image plane. This corrects the monochromatic aberrations to improve the imaging quality. Analysis of the two-dimensional aberration-corrected information in the image plane enables the 3D coordinates of the object to be determined with a measured relative accuracy of 0.60%–1.31%. We also demonstrate the effectiveness of the metalens array for arbitrary incident polarization states. Our approach is single-shot, compact, aberration-corrected, polarization-insensitive, and paves the way for future integrated photonic robotic vision systems and intelligent sensing platforms that are feasible on the submillimeter scale, such as face recognition, autonomous vehicles, microrobots, and wearable intelligent devices. © 2020 Optical Society of America under the terms of the OSA Open Access Publishing Agreement

<https://doi.org/10.1364/OPTICA.406039>

1. INTRODUCTION

Optical imaging and positioning systems play a key role in modern optics and photonics, which promotes the burgeoning development of technologies such as those in cameras, microscopes, optical radars, and visual sensors [1–3]. Traditionally, the basic elements in imaging and positioning systems, such as lenses, are bulky constructions, and shrinking their size with the view of incorporation into integrated optics presents a challenge. In recent years, metalenses have garnered great interest in the scientific community owing to their comparable or superior performance compared with conventional optical components [4–6]. By elaborately tailoring the shapes of nanostructures, the resonant electromagnetic modes can be locally controlled on a subwavelength scale [7–11], which makes the metalenses a versatile platform to control the wavefront pixel by pixel [12–17]. Taking advantage of the multidimensional manipulation of optical fields with nanostructures [18–21], researchers have developed numerous intriguing metalens designs such as those in high-resolution spectroscopy [22], light-field cameras [23], quantitative phase gradient microscopy [24], and optical depth sensors [25]. These inspiring approaches indicate significant possibilities enabled by artificial nanostructures to achieve integrated photonic systems. To date, it is still challenging to realize

accurate three-dimensional (3D) positioning of an arbitrary object with devices of a compact size, especially for positioning that is prone to imaging aberrations.

The disadvantage of single-layer metalenses is their evident aberrations (except for spherical aberration) because these lenses are usually fabricated on a flat surface with an artificially designed local phase abrupt [4,26]. By engineering the phase dispersions of the nanostructures at different wavelengths [27–30], or by designing multistructures operating at different wavelengths [31], researchers have realized achromatic metalenses in the visible region. Monochromatic imaging aberrations have also been studied in the metalens scheme using several methods. For example, coma can be corrected by patterning metalens building blocks on a curved surface [32,33]. Astigmatism and the focal length can be simultaneously controlled by tuning the elastomer on which the metalens is fabricated [34]. By employing a corrector metasurface paired with a metalens, monochromatic aberrations can also be corrected in the near-infrared and visible regions [35,36]. This doublet metalens design has also been employed in other photonic devices such as retroreflectors [37]. However, current designs require either challenging or complex fabrication methods. Another approach to correcting the imaging aberrations is

to arbitrarily control the angular dispersion of the nanostructures [17,38], which is also problematic because the intensity and phase of the scattered light of nanostructures would both have to be elaborately manipulated in an imaging system for a broad range of incident angles.

Here, we introduce a metalens array to realize optical positioning and adopt a gradient descent algorithm [39,40] to correct the monochromatic aberrations in the imaging system. Taking advantage of the versatile wavefront-shaping capability of metalenses, we employ titanium dioxide nanopillars to build a metalens array operating in the visible region. This metalens array can image a target object at different locations containing different imaging and aberration information. In contrast to approaches that employ doublet [35] or curved [33] designs, we utilize the cross-correlation-based gradient descent (CCGD) algorithm to analyze and combine the information from different parts of the image, and form a reconstructed aberration-corrected image with only a planar single-layer metasurface that does not require complex fabrication. The 3D coordinates and the size of the target object can be simultaneously derived from the single-shot two-dimensional (2D) information in the image plane with high accuracy, and the total size of the metalens array is only 379.5 μm . In addition, the proposed design is also polarization-insensitive, which means it can be readily applied in practical data-driven imaging and positioning applications.

2. CONCEPT OF POSITIONING BASED ON METALENS ARRAYS

A metalens array consists of periodic metalenses, which are able to focus and image the incident light in different areas without overlapping, as shown in Fig. 1(a). Note that, although we employed three close-packed hexagonal metalenses as an implementation example, the proposed scheme does not limit the metalenses to a specific number. The metalens array captures three images of object “A” in the image plane [Fig. 1(b)]. In the laboratory coordinate frame of the metalens array, “A” is located at $A'(S_{\perp}, S_{//})$, where S_{\perp} and $S_{//}$ are the vertical (along the $+z$ direction) and horizontal coordinates of “A”, respectively. Note that $S_{//}$ can be decomposed into two orthogonal components, $S_{//x}$ and $S_{//y}$.

For simplicity, we only use $S_{//}$ to quantify the 2D coordinates in the object plane. In the local coordinates frame of the metalens L_i , “A” is located at $a_i(S_{\perp}, id + S_{//})$, where d is the periodicity of the metalens array (here d is also the size of the metalens). The coordinates of the image in the local frame can be written as $a'_i(S'_{\perp}, M(id + S_{//}))$, and in the laboratory frame, the image is located at $A'_i(S'_{\perp}, M(id + S_{//}) - id)$, where M is the magnification of the metalens, and S'_{\perp} is the image distance. The magnification can be calculated using $M = -(D - d)/d$, where D is the periodicity of the images, and the negative sign indicates a reverse image. Following the relations between the coordinates of the object and the images, the object distance and the horizontal displacement can be calculated as

$$S_{\perp} = fD/(D - d), \quad (1)$$

$$S_{//} = \Delta(D - d)/d, \quad (2)$$

where f is the focal length of the metalens. Thus, the 3D coordinates of the object (or an arbitrary single point) could be positioned simply by analyzing the 2D image in the image plane.

A realistic monochromatic imaging system usually experiences different imaging aberrations, such as image distortion, spherical aberration, coma, astigmatism, and field curvature. The aberrations of the proposed spherical-aberration-free metalens array can be categorized into two types: one is the distortion resulting in the radial transformations of the image, and the other causes poorly resolved images in the image plane, with defects such as coma, astigmatism, and field curvature, especially for components with a high spatial frequency. The first type of aberration can be corrected by revising the lower order of radial components [41] in the image,

$$\Delta x = x_r (k_1 r^2 + k_2 r^4), \quad (3)$$

$$\Delta y = y_r (k_1 r^2 + k_2 r^4), \quad (4)$$

where $(\Delta x, \Delta y)$ is the correction of the distorted image, (x_r, y_r) are the coordinates of a pixel in the image with the original point located at the distortion center, k_1 and k_2 are two parameters to

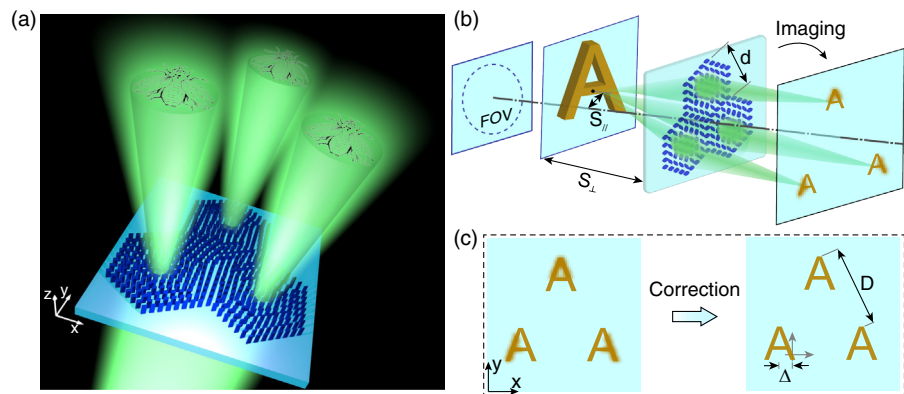


Fig. 1. Design of the single-shot positioning metalens array and its operation principle. (a) Schematic of the ideal metalens array that can form different images in the image plane without considering imaging aberrations; (b) illustration of the positioning system that can locate the 3D coordinates of an arbitrary object “A”. The horizontal and vertical coordinates $S_{//}$ and S_{\perp} can be acquired from captured images containing aberrations. The length d is the periodicity of the metalens array and is the diameter of the incircle of the metalens. The blue dashed circle indicates the working FOV of the system, which reaches 49.6° obtained from experiments. (c) The imaging aberrations in the image plane can be corrected following the CCGD algorithm, leading to accurate measurement of the characteristic quantities D (periodicity of the images) and Δ (horizontal distance in the image plane).

be optimized, and r is the distance between the pixel and the distortion center. The three images of the object possess different information, which provides the possibility of reconstructing new images of which the aberrations have been corrected [Fig. 1(c)]. We employed the CCGD algorithm to simultaneously correct the above-mentioned two types of aberrations, which is discussed in detail in the following sections.

3. SAMPLE FABRICATION AND CHARACTERIZATION

We used titanium dioxide nanopillars as the building blocks and built a prototype metalens array [Figs. 2(a)–2(d)]. By controlling the orientation angle θ of the nanopillars, the wavefront of the metalens can be locally manipulated by the Pancharatnam–Berry phase $\phi = 2\sigma\theta$ [42,43], where $\sigma = \pm 1$ represents the helicity of light and is controlled by a polarizer and a quarter-wave plate (P1 and QW1 in Fig. S4 in Supplement 1). The nanopillars, which are 550 nm high, can be readily fabricated using the standard atomic layer deposition method [44] by using single-step lithography without challenging the fabrications (note S1 in Supplement 1). The quadrangular nanopillars with a chamfer length of

40 nm maintained high transmission efficiency (Fig. S1 in Supplement 1), which is important for realistic applications. The diameter of the fabricated metalens is $d = 189.75 \mu\text{m}$, and the designed focal length is $165 \mu\text{m}$ at the operating wavelength of 532 nm. The measured diffraction-limited focusing profiles are shown in Fig. 2(e) (see Fig. S2 in Supplement 1 for the evolution of focusing at different cut planes). The light distribution near the focal point is not angular symmetric because of the close-packed arrangement of hexagonal metalenses. Such an arrangement guarantees a high fill factor in the device area, and the astigmatism caused by the asymmetry along with other types of aberrations can be further corrected by a postprocessing algorithm.

Basically, the positioning properties highly rely on the imaging qualities in any optical positioning system because the positioning information is extracted from the optical path or light distributions. The positioning accuracy decreases if the imaging is affected by aberrations, especially for large incident angles and off-axis imaging. As shown in Fig. 2(f), for the single-layer dielectric metalens, the aberrations significantly increase when the incident angles become larger. The full width at half-maximum of the focusing intensity gradually increases as the incident angle increases, which exhibits the intensity distribution symmetry broken in the oblique

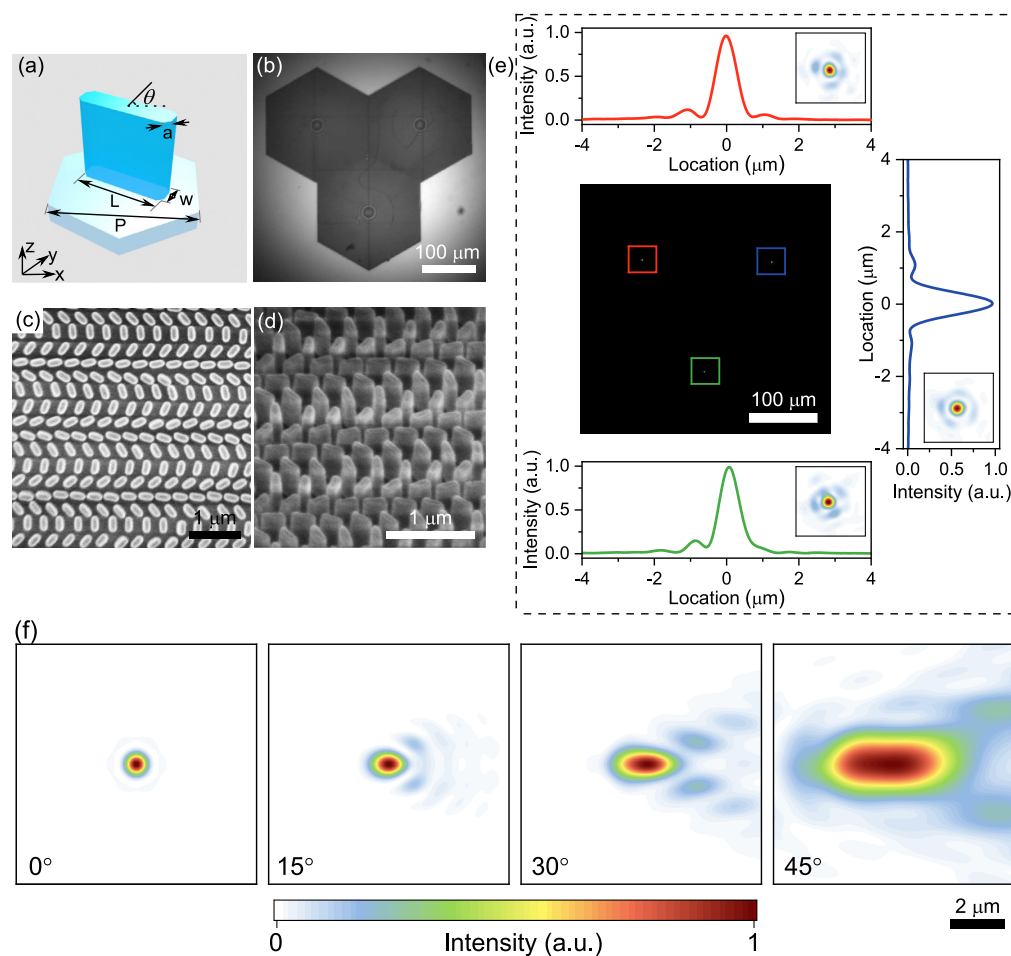


Fig. 2. Fabrication and characterization of the metalens array. (a) The building block of the metalens consists of titanium dioxide nanopillars with a height of 550 nm fabricated on a fused silica substrate. The chamfer length of the nanopillars is $a = 40 \text{ nm}$, and the size of the hexagonal lattice is 330 nm . (b) Photographic image of the metalens array taken by a CCD camera on a microscope; (c) and (d) scanning electron micrographs of the fabricated metalens: (c) top and (d) tilted views; (e) measured intensity distribution of the metalens array at the focal plane. The solid red, blue, and green lines indicate the light distributions at three different focal points. Insets, measured intensity profiles near different focal points. (f) Simulated intensity distributions in the focal plane showing the evolution of aberrations for different incident angles of 0° , 15° , 30° , and 45° (left to right).

incident direction, especially for incident angles greater than 30° . In contrast to directly correcting the focusing aberrations with doublet metalens design [35,36] or other fabrication-challenging designs, we analyzed the imaging information in the image plane of the metalens arrays to simultaneously obtain aberration-corrected images and highly accurate positioning coordinates of the object. The object in our experiments is shown in Fig. S3 in Supplement 1. To obtain the imaging properties of the metalens array, we used a custom-built scanning system to control the position of the object and capture the final images (Fig. S4 in Supplement 1).

4. IMPLEMENTATION OF VERTICAL AND HORIZONTAL POSITIONING WITH THE CCGD ALGORITHM

The image of S1 (a binary bee), which is also the object to be positioned by the metalens array, is shown in Fig. 3(a). The raw images for different object distances in the image plane show apparent imaging aberrations, which means losing the high spatial Fourier information, especially near the edge of the field of view (FOV) [Fig. 3(c(i))]. Several types of imaging aberrations exist, such as

coma, astigmatism, distortion, and field curvature. Basically, the imaging aberration becomes larger and more complex as the image area progressively moves away from the center of the image, which means a lower spatial frequency with distortion. We ignored the areas affected by dramatic aberrations in each image part, and used only the low-aberration areas, that is, zones A, B, and C in Fig. 3(c) to reconstruct the image. This not only alleviates the negative effects of aberrations on the reconstructed image, but also reduces the difficulties associated with parameter optimization. For example, we only need to consider the first and second terms in the distortion expansion equation to correct the radial distortion, rather than calculating more terms and tangential distortions in areas farther away from the center of the image [45,46]. The combination of different areas of the image captured by the metalens array enables a reconstructed image, of which the aberrations have been corrected and the spatial frequency has been improved [Fig. 3(c(ii))]. Instead of analyzing each type of aberration, here we employed an algorithm to correct different types of aberrations altogether because these aberrations negatively affect the image resolution of different parts of the image in different ways.

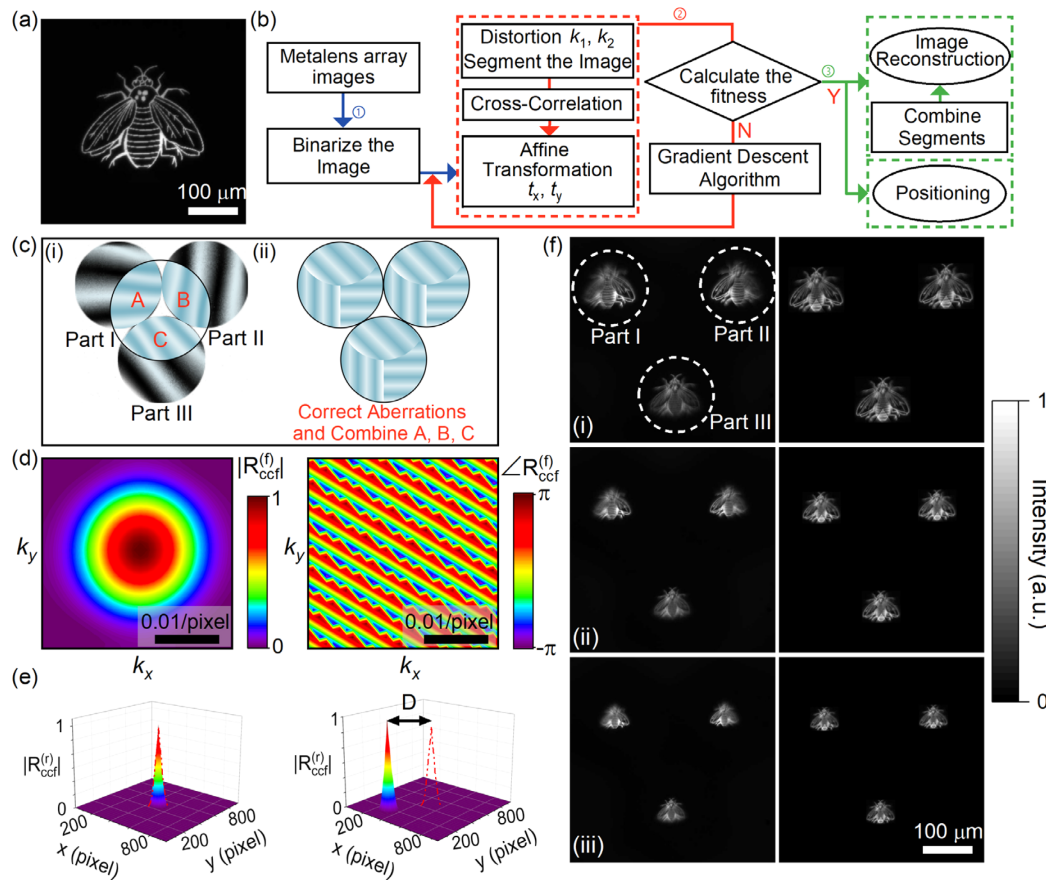


Fig. 3. Imaging and positioning experiments based on the metalens array. (a) Image S1 used as the object of the positioning metalens; (b) flow chart of the CCGD algorithm, where step 1 is image preprocessing, step 2 is the CCGD algorithm to obtain the spatial relations between different parts of the image and to correct the imaging aberrations, and step 3 is to realize spatial positioning and to obtain the reconstructed aberration-corrected image; (c) schematic illustration of the aberration-corrected algorithm. (i) The raw image contains clearer zones (A, B, and C) with high spatial frequency and little distortion, and contains indistinct areas (black) with low spatial frequency and substantial distortion. (ii) By combining A, B, C, and correcting the aberrations of the image, the overall spatial frequency is improved. (d) Amplitude and phase distributions of $R_{ccf}^{(f)}$ between Part I and Part III in Fourier space with an object distance of $825.0 \mu\text{m}$; (e) amplitude distributions of $R_{ccf}^{(r)}$ between Part I and Part I (left), and between Part I and Part III (right) in the pixel space with an object distance of $825.0 \mu\text{m}$; (f) the original (left) and recovered (right) images of the metalens array. The object distance is set as (i) $495.0 \mu\text{m}$, (ii) $660.0 \mu\text{m}$, and (iii) $825.0 \mu\text{m}$, respectively. The dashed white circles indicate three different parts of the image (see Visualization 1 and Visualization 2).

This excludes distortion, which can be corrected by optimizing the parameters in Eqs. (3) and (4).

As shown in the flow chart in Fig. 3(b), we first segment the raw images into three different parts in step 1, which are then compared and merged in the following steps. The size and shape of each part are not specifically limited because each part contains a complete image (i.e., a single complete bee). We also binarize the raw images into “0” and “1” to eliminate the gray information, whereas the shape information in the images is preserved. In step 2, we consider (k_1, k_2) and (t_x, t_y) as the key parameters for distortion in the images and translation factors between different parts of the images, respectively. The CCGD algorithm was employed to combine different parts of the images. We calculated the cross-correlation functions to obtain the overall translation relations between different image parts. For example, for two arbitrary image parts P_a and P_b , which are related to $P_b = P_a(x - t_x, y - t_y)$, the cross-correlation functions in the Fourier space and in real space can be written as

$$R_{cf}^{(f)}(k_x, k_y) = \mathcal{F}(P_a) \mathcal{F}^*(P_a) \exp[2\pi j(k_x t_x + k_y t_y)], \quad (5)$$

$$R_{cf}^{(r)}(x, y) = G(x - t_x, y - t_y), \quad (6)$$

where $G(x, y)$ is the inverse Fourier transform of $\mathcal{F}(P_a)\mathcal{F}^*(P_a)$. The maximum value of $|R_{cf}^{(r)}|$ is located at (t_x, t_y) , which characterizes the translation relationship between P_a and P_b (see Section 2 in Supplement 1). The calculated cross-correlation functions for an object distance of 825.0 μm are shown in Figs. 3(d) and 3(e). The optimization is conducted iteratively until the convergence condition is reached. In our framework, the fitness function is defined as

$$J_{31} = \frac{\sum_{i=1}^{m_1} \sum_{j=1}^{n_1} |P'_1(i, j) - P_3(i, j)|^2}{m_1 \times n_1}, \quad (7)$$

$$J_{23} = \frac{\sum_{i=1}^{m_2} \sum_{j=1}^{n_2} |P'_2(i, j) - P_3(i, j)|^2}{m_2 \times n_2}, \quad (8)$$

where P'_1 and P'_2 are the images of Parts I and II, respectively, after translation to overlap with the image of Part III (P_3) during the combination process. Step 3 involves the combination of different parts of the raw images when the convergence condition is met, and the missing information in each part of the image is also completed [right column in Fig. 3(f)]. The 3D coordinates and the size of the object can be calculated according to Eqs. (1) and (2).

The quality of the reconstructed images is greatly improved both in terms of sharpness and completeness, which guarantees that the geometric parameters could be more accurately acquired from the images. More raw and reconstructed images can be found in Fig. S6 in Supplement 1. As shown in Fig. 4, the recovered vertical and horizontal coordinates of the object are in good agreement with those of the experimental setups. The measured relative positioning accuracy (RPA) is in the range of 0.60%–1.31%, which reaches the state-of-the-art level owing to the aberration-correcting process based on the metalens arrays. Compared with the positioning results without correcting the aberrations, the positioning accuracy increases several times (gray areas in Fig. 4), especially for S_{\perp} at long object distances and $S_{//}$ at short object distances.

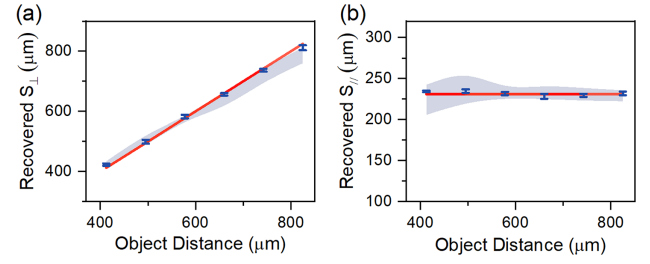


Fig. 4. Recovered (a) vertical distance S_{\perp} and (b) horizontal distance $S_{//}$ compared with the experimental setup (red lines) for different object distances. Error bars represent the standard deviations of the measured distances calculated from the optimized D between different image parts. The gray areas indicate the recovered vertical/horizontal distances without adopting the CCGD algorithm.

The positioning accuracy usually increases as the object distance decreases when the image aberrations are ignored. The metalens array can operate within an FOV of 49.6° with an RPA below 1.50% for off-axis imaging, even though the original image is poorly resolved and incomplete for large incident angles (Fig. S11). This high-accuracy positioning can be attributed to the cross-correlation method, which combines the overall information in each image part, leading to accurate positioning on condition that certain information is valuable for positioning. These results demonstrate the effectiveness of simultaneously improving the imaging and positioning performance based on the proposed aberration-correcting method. To quantify the correction of aberrations, we also calculated the overall sharpness of each image using the Tenengrad function method (Fig. S12 in Supplement 1). As a result, the sharpness of the reconstructed images increased significantly, especially for short object distances (setup #1), in which case the image is affected by obvious aberrations owing to the off-axis incidence.

5. ANALYSIS OF THE POLARIZATION SENSITIVITY AND THE POSITIONING ACCURACY

In actual applications, the polarization states of the incident light could easily limit the applicability of the device. To examine the incident polarization tolerance of the metalens array, we removed the QW1 and the P1, considering that the polarization of the lamp beam is similar to that of natural light. The proposed strategy was ultimately found to be effective for both situations, and the accuracy of positioning remains almost the same as that of the original setup [Figs. 5(a)–5(c)]. This tolerance of polarization can be attributed to the analyzer pair (QW2 and P2), which filters the left-handed circularly polarized components in the background. On the other hand, the background noise could also be easily removed by the postprocessing algorithm. These interesting results demonstrate that the proposed prototype of the metalens array functions well for arbitrary incident polarizations. The detailed raw and reconstructed images are shown in Figs. S7 and S8 in Supplement 1. The RPA of the metalens array could be further quantified given the location of the object and design parameters of the metalens array (note S3 in Supplement 1),

$$\left| \frac{\Delta S_{\perp}}{S_{\perp}} \right| = \frac{\frac{S_{\perp}}{f} + \frac{f}{S_{\perp}} - 2}{d} |\Delta D|, \quad (9)$$

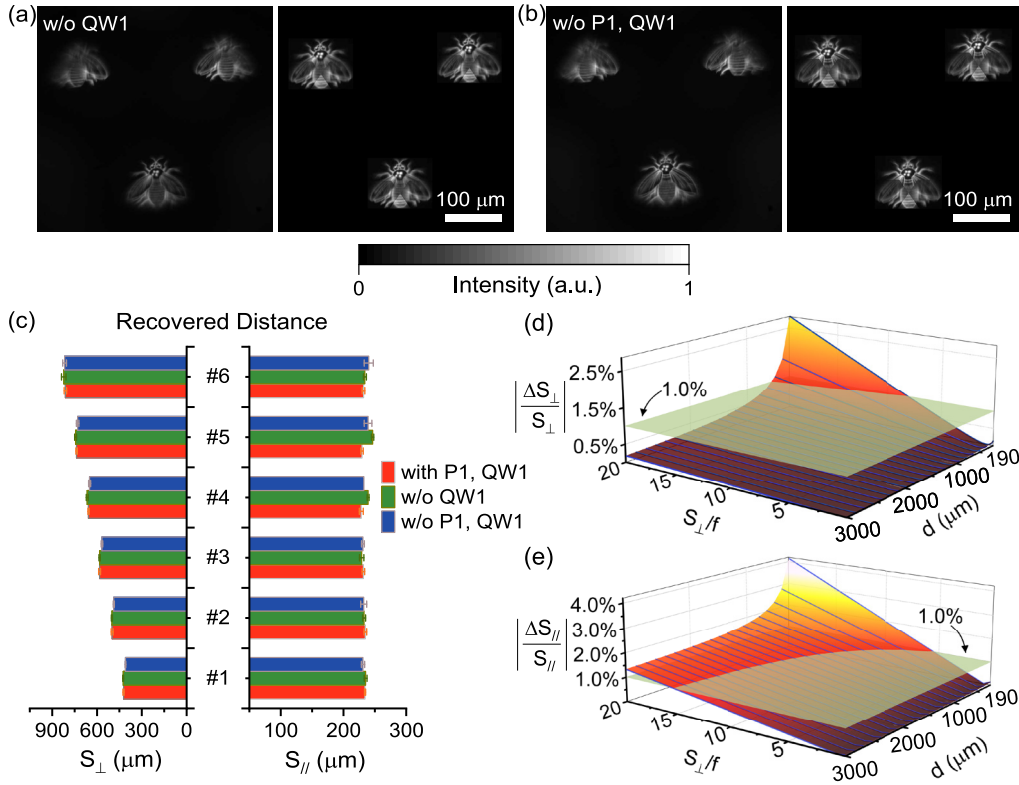


Fig. 5. Positioning for different incident polarization states and positioning accuracy for different setups. (a) and (b) The original (left) and recovered (right) images of the metalens array (a) without QW1 and (b) without P1 and QW1 for an object distance of 495.0 μm. The results indicate that the proposed positioning system does not have limitations with respect to incident polarization. (c) Comparison of recovered vertical and horizontal distances between different incident polarization states. (d) and (e) Calculated RPA in the (d) vertical and (e) horizontal directions as a function of the relative object length and the size of the metalens. The semitransparent green planes indicate the areas for RPA of 1.0% as a reference in the vertical and horizontal directions, respectively.

$$\left| \frac{\Delta S_{\parallel}}{S_{\parallel}} \right| = \frac{(d + S_{\parallel}) |S_{\perp} - f|}{f d S_{\parallel}} |\Delta D|, \quad (10)$$

where ΔD is the measurement accuracy in the image plane and can be estimated from the measured $|\Delta S_{\perp}/S_{\perp}|$ as $\Delta D \simeq 0.3 \mu\text{m}$. This accuracy closely approximates the diffraction limit at the operating wavelength of 532 nm, demonstrating the effectiveness of the proposed aberration-correcting scheme. As shown in Figs. 5(d) and 5(e), the RPA is a function of the size of the metalens d , and the normalized object distance S_{\perp}/f . For simplicity, we set S_{\parallel} as 500 μm in the calculation (see Fig. S9 for the RPA with different S_{\parallel}). We selected a constant RPA of 1.0% as a reference and threshold in the vertical and horizontal directions for comparison with the proposed metalens array design. We discovered that the RPA threshold can be easily achieved with a suitable metalens design operating in a long object distance range. Even for realistic applications such as robotic vision with object distances as long as several meters, the RPA threshold can be easily achieved with suitable metalens design, such as enlarging the diameters and extending the focal lengths of the metalenses. However, the increase in the focal length could lead to a lower numerical aperture if the size of the metalens is set in advance. Fortunately, recent developments in dynamic and tunable metasurfaces have provided possibilities for fast tuning of the focal lengths of metalenses [47,48], which may balance the trade-off between positioning and imaging. This result shows that the proposed design can be applied across a wide operating range with high positioning accuracy. The postprocessing time of the

CCGD algorithm depends on the size of the image because the algorithm needs to perform matrix operations during its iteration. The typical postprocessing time of an image of 300×300 pixels is approximately several seconds using an Intel i5-9400F CPU in a commercial laptop. More details about the postprocessing time for different image sizes and the related RPA can be found in Fig. S10 in Supplement 1. Postprocessing can be further accelerated by employing a graphics processing unit or by optimizing the code.

6. SUMMARY AND CONCLUSION

Note that high-accuracy positioning results are achieved by the proposed metalens scheme, but not by the measurement setup. The accuracy of the imaging translation stage is approximately 10 μm, which can be easily realized in realistic applications. The size of the metalens in our prototype is only $d = 189.75 \mu\text{m}$, which means that the vertical positioning accuracy could be further improved by enlarging the size of the metalens [Fig. 5(d)]. Current fabrication techniques enable metalenses to be fabricated on the millimeter scale. Compared with other optical positioning methods based on lens designs, our strategy provides convenient aberration-corrected performance, which guarantees significantly improved accuracy in both imaging and positioning. Compared with positioning via mechanical platforms, this method relies on the optical intensity of the images, which is only fundamentally limited by the Abbe diffraction limit. Our strategy does not impose specific limitations in terms of the working distances, and the

depth-sensing accuracy can be improved 4 to 8 times compared with previous results [25] (calculated with similar setups such as the device size and the focal length). The proposed method uses larger and higher numerical-aperture metalenses and employs an aberration-correcting algorithm, which can significantly improve the quality of the reconstructed images, enlarge the FOV, and correct the imaging aberrations [23]. The proposed scheme can also be extended to real 3D objects by employing the spectral tomographic imaging method [26]. Taking advantage of the chromatic aberration of a metalens, which provides different focal lengths for different operating wavelengths, this spectral tomographic imaging method can be readily applied in our system to realize fast spectral refocusing and further obtain different information on the different cutting planes of the 3D object.

In conclusion, we proposed and experimentally demonstrated the design and working principle for single-shot optical positioning with a metalens array. Instead of correcting the imaging aberrations with complex fabrication techniques, we employed the CCGD algorithm to analyze and combine different parts in the image plane of the metalenses and to complete the missing information in each image part. The proposed algorithm facilitates the correction of different imaging aberrations of the metalens array, such as distortion, coma, astigmatism, and field curvature. By analyzing the 2D information and marking featured points in the aberration-corrected image plane, the 3D coordinates of the object can be further derived with the measured relative accuracy ranging from 0.60% to 1.31% to reach the state-of-the-art level. The location of the object is not limited in any specific way, and the positioning accuracy can be further improved by enlarging the size of the metalens. The abilities of the metalens array working under arbitrary polarization states were also demonstrated to realize the positioning of the object. The proposed scheme is compact, single-shot, passive, and demonstrates the potential use of the dielectric metalens platform in miniaturized positioning systems and compact visual sensors with high accuracy.

Funding. National Key Research and Development Program of China (2016YFA0301102, 2017YFA0303800); China National Funds for Distinguished Young Scientists (11925403); National Natural Science Foundation of China (11904183, 11904181, 11974193, 91856101, 11774186, 21421001); Natural Science Foundation of Tianjin City for Distinguished Young Scientists (18JJCJC45700); National Postdoctoral Program for Innovative Talents (BX20180148); China Postdoctoral Science Foundation (2018M640224, 2018M640229).

Acknowledgment. Support from the ACT node of the Australian National Fabrication Facility in the form of nanofabrication of the metalens is gratefully acknowledged.

Disclosures. The authors declare no conflicts of interest.

See [Supplement 1](#) for supporting content.

[†]These authors contributed equally to this work.

REFERENCES

- B. E. A. Saleh and M. C. Teich, *Fundamentals of Photonics* (Wiley, 1991).
- J. Geng, "Structured-light 3D surface imaging: a tutorial," *Adv. Opt. Photon.* **3**, 128–160 (2011).
- F. Mayingier, *Optical Measurements: Techniques and Applications* (Springer, 2013).
- F. Aieta, P. Genevet, M. A. Kats, N. Yu, R. Blanchard, Z. Gaburro, and F. Capasso, "Aberration-free ultrathin flat lenses and axicons at telecom wavelengths based on plasmonic metasurfaces," *Nano Lett.* **12**, 4932–4936 (2012).
- M. Khorasaninejad, W. T. Chen, R. C. Devlin, J. Oh, A. Y. Zhu, and F. Capasso, "Metalenses at visible wavelengths: diffraction-limited focusing and subwavelength resolution imaging," *Science* **352**, 1190–1194 (2016).
- H. W. Liang, A. Martins, B. H. V. Borges, J. Y. Zhou, E. R. Martins, J. T. Li, and T. F. Krauss, "High performance metalenses: numerical aperture, aberrations, chromaticity, and trade-offs," *Optica* **6**, 1461–1470 (2019).
- K. Koshelev, S. Kruk, E. Melik-Gaykazyan, J. H. Choi, A. Bogdanov, H. G. Park, and Y. Kivshar, "Subwavelength dielectric resonators for nonlinear nanophotonics," *Science* **367**, 288–292 (2020).
- A. Zhan, R. Gibson, J. Whitehead, E. Smith, J. R. Hendrickson, and A. Majumdar, "Controlling three-dimensional optical fields via inverse Mie scattering," *Sci. Adv.* **5**, eaax4769 (2019).
- H. X. Xu, G. Hu, Y. Li, L. Han, J. Zhao, Y. Sun, F. Yuan, G. M. Wang, Z. H. Jiang, X. Ling, T. J. Cui, and C. W. Qiu, "Interference-assisted kaleidoscopic meta-plexer for arbitrary spin-wavefront manipulation," *Light: Sci. Appl.* **8**, 3 (2019).
- S. Liu, A. Vaskin, S. Campione, O. Wolf, M. B. Sinclair, J. Reno, G. A. Keeler, I. Staude, and I. Brener, "Huygens' metasurfaces enabled by magnetic dipole resonance tuning in split dielectric nanoresonators," *Nano Lett.* **17**, 4297–4303 (2017).
- G. Li, S. Zhang, and T. Zentgraf, "Nonlinear photonic metasurfaces," *Nat. Rev. Mater.* **2**, 17010 (2017).
- S. Liu, T. J. Cui, Q. Xu, D. Bao, L. Du, X. Wan, W. X. Tang, C. Ouyang, X. Y. Zhou, H. Yuan, H. F. Ma, W. X. Jiang, J. Han, W. Zhang, and Q. Cheng, "Anisotropic coding metamaterials and their powerful manipulation of differently polarized terahertz waves," *Light: Sci. Appl.* **5**, e16076 (2016).
- S. Chen, Z. Li, W. Liu, H. Cheng, and J. Tian, "From single-dimensional to multidimensional manipulation of optical waves with metasurfaces," *Adv. Mater.* **31**, 1802458 (2019).
- Q. Wang, E. T. F. Rogers, B. Gholipour, C.-M. Wang, G. Yuan, J. Teng, and N. I. Zheludev, "Optically reconfigurable metasurfaces and photonic devices based on phase change materials," *Nat. Photonics* **10**, 60–65 (2015).
- E. Maguid, I. Yulevich, D. Veksler, V. Kleiner, M. L. Brongersma, and E. Hasman, "Photonic spin-controlled multifunctional shared-aperture antenna array," *Science* **352**, 1202–1206 (2016).
- H. Liang, Q. Lin, X. Xie, Q. Sun, Y. Wang, L. Zhou, L. Liu, X. Yu, J. Zhou, T. F. Krauss, and J. Li, "Ultrahigh numerical aperture metalens at visible wavelengths," *Nano Lett.* **18**, 4460–4466 (2018).
- W. Liu, Z. Li, H. Cheng, C. Tang, J. Li, S. Zhang, S. Chen, and J. Tian, "Metasurface enabled wide-angle Fourier lens," *Adv. Mater.* **30**, 1706368 (2018).
- A. Arbabi, Y. Horie, M. Bagheri, and A. Faraon, "Dielectric metasurfaces for complete control of phase and polarization with subwavelength spatial resolution and high transmission," *Nat. Nanotechnol.* **10**, 937–943 (2015).
- J. P. Balthasar Mueller, N. A. Rubin, R. C. Devlin, B. Groever, and F. Capasso, "Metasurface polarization optics: independent phase control of arbitrary orthogonal states of polarization," *Phys. Rev. Lett.* **118**, 113901 (2017).
- H. X. Xu, G. Hu, L. Han, M. Jiang, Y. Huang, Y. Li, X. Yang, X. Ling, L. Chen, J. Zhao, and C. W. Qiu, "Chirality-assisted high-efficiency metasurfaces with independent control of phase," *Adv. Opt. Mater.* **6**, 1801479 (2018).
- M. Kim and G. V. Eleftheriades, "Design and experimental demonstration of impedance-matched circular-polarization-selective surfaces with spin-selective phase modulations," *Phys. Rev. Appl.* **13**, 014009 (2020).
- M. Khorasaninejad, W. T. Chen, J. Oh, and F. Capasso, "Super-dispersive off-axis meta-lenses for compact high-resolution spectroscopy," *Nano Lett.* **16**, 3732–3737 (2016).
- R. J. Lin, V. C. Su, S. Wang, M. K. Chen, T. L. Chung, Y. H. Chen, H. Y. Kuo, J. W. Chen, J. Chen, Y. T. Huang, J. H. Wang, C. H. Chu, P. C. Wu, T. Li, Z. Wang, S. Zhu, and D. P. Tsai, "Achromatic metalens array for full-colour light-field imaging," *Nat. Nanotechnol.* **14**, 227–231 (2019).
- H. Kwon, E. Arbabi, S. M. Kamali, M. Faraji-Dana, and A. Faraon, "Single-shot quantitative phase gradient microscopy using a system of multifunctional metasurfaces," *Nat. Photonics* **14**, 109–114 (2019).

25. Q. Guo, Z. Shi, Y. W. Huang, E. Alexander, C. W. Qiu, F. Capasso, and T. Zickler, "Compact single-shot metalens depth sensors inspired by eyes of jumping spiders," *Proc. Natl. Acad. Sci. USA* **116**, 22959–22965 (2019).
26. C. Chen, W. Song, J. W. Chen, J. H. Wang, Y. H. Chen, B. Xu, M. K. Chen, H. Li, B. Fang, J. Chen, H. Y. Kuo, S. Wang, D. P. Tsai, S. Zhu, and T. Li, "Spectral tomographic imaging with aplanatic metalens," *Light: Sci. Appl.* **8**, 99 (2019).
27. M. Khorasaninejad, Z. Shi, A. Y. Zhu, W. T. Chen, V. Sanjeev, A. Zaidi, and F. Capasso, "Achromatic metalens over 60 nm bandwidth in the visible and metalens with reverse chromatic dispersion," *Nano Lett.* **17**, 1819–1824 (2017).
28. S. Wang, P. C. Wu, V. C. Su, Y. C. Lai, C. Hung Chu, J. W. Chen, S. H. Lu, J. Chen, B. Xu, C. H. Kuan, T. Li, S. Zhu, and D. P. Tsai, "Broadband achromatic optical metasurface devices," *Nat. Commun.* **8**, 187 (2017).
29. W. T. Chen, A. Y. Zhu, V. Sanjeev, M. Khorasaninejad, Z. Shi, E. Lee, and F. Capasso, "A broadband achromatic metalens for focusing and imaging in the visible," *Nat. Nanotechnol.* **13**, 220–226 (2018).
30. S. Wang, P. C. Wu, V. C. Su, Y. C. Lai, M. K. Chen, H. Y. Kuo, B. H. Chen, Y. H. Chen, T. T. Huang, J. H. Wang, R. M. Lin, C. H. Kuan, T. Li, Z. Wang, S. Zhu, and D. P. Tsai, "A broadband achromatic metalens in the visible," *Nat. Nanotechnol.* **13**, 227–232 (2018).
31. O. Avayu, E. Almeida, Y. Prior, and T. Ellenbogen, "Composite functional metasurfaces for multispectral achromatic optics," *Nat. Commun.* **8**, 14992 (2017).
32. N. Bokor and N. Davidson, "Aberration-free imaging with an aplanatic curved diffractive element," *Appl. Opt.* **40**, 5825–5829 (2001).
33. F. Aieta, P. Genevet, M. Kats, and F. Capasso, "Aberrations of flat lenses and aplanatic metasurfaces," *Opt. Express* **21**, 31530–31539 (2013).
34. A. She, S. Zhang, S. Shian, D. R. Clarke, and F. Capasso, "Adaptive metalenses with simultaneous electrical control of focal length, astigmatism, and shift," *Sci. Adv.* **4**, eaap9957 (2018).
35. A. Arbabi, E. Arbabi, S. M. Kamali, Y. Horie, S. Han, and A. Faraon, "Miniature optical planar camera based on a wide-angle metasurface doublet corrected for monochromatic aberrations," *Nat. Commun.* **7**, 13682 (2016).
36. B. Groever, W. T. Chen, and F. Capasso, "Meta-lens doublet in the visible region," *Nano Lett.* **17**, 4902–4907 (2017).
37. A. Arbabi, E. Arbabi, Y. Horie, S. M. Kamali, and A. Faraon, "Planar metasurface retroreflector," *Nat. Photonics* **11**, 415–420 (2017).
38. M. Qiu, M. Jia, S. Ma, S. L. Sun, Q. He, and L. Zhou, "Angular dispersions in terahertz metasurfaces: physics and applications," *Phys. Rev. Appl.* **9**, 054050 (2018).
39. K. Yamazoe, I. Mochi, and K. A. Goldberg, "Gradient descent algorithm applied to wavefront retrieval from through-focus images by an extreme ultraviolet microscope with partially coherent source," *J. Opt. Soc. Am. A* **31**, B34–B43 (2014).
40. D. P. Mandic, "A generalized normalized gradient descent algorithm," *IEEE Signal Process. Lett.* **11**, 115–118 (2004).
41. Z. Zhang, "A flexible new technique for camera calibration," *IEEE Trans. Pattern Anal. Mach. Intell.* **22**, 1330–1334 (2000).
42. X. Chen, L. Huang, H. Muhlenbernd, G. Li, B. Bai, Q. Tan, G. Jin, C. W. Qiu, S. Zhang, and T. Zentgraf, "Dual-polarity plasmonic metalens for visible light," *Nat. Commun.* **3**, 1198 (2012).
43. G. Li, S. Chen, N. Pholchai, B. Reineke, P. W. Wong, E. Y. Pun, K. W. Cheah, T. Zentgraf, and S. Zhang, "Continuous control of the non-linearity phase for harmonic generations," *Nat. Mater.* **14**, 607–612 (2015).
44. R. C. Devlin, M. Khorasaninejad, W. T. Chen, J. Oh, and F. Capasso, "Broadband high-efficiency dielectric metasurfaces for the visible spectrum," *Proc. Natl. Acad. Sci. USA* **113**, 10473–10478 (2016).
45. S. Shah and J. K. Aggarwal, "Intrinsic parameter calibration procedure for a (high-distortion) fish-eye lens camera with distortion model and accuracy estimation," *Pattern Recogn.* **29**, 1775–1788 (1996).
46. V. N. Mahajan, *Optical Imaging and Aberrations* (SPIE, 1998).
47. A. Lininger, A. Y. Zhu, J. S. Park, G. Palermo, S. Chatterjee, J. Boyd, F. Capasso, and G. Strangi, "Optical properties of metasurfaces infiltrated with liquid crystals," *Proc. Natl. Acad. Sci. USA* **117**, 20390–20396 (2020).
48. E. Arbabi, A. Arbabi, S. M. Kamali, Y. Horie, M. Faraji-Dana, and A. Faraon, "MEMS-tunable dielectric metasurface lens," *Nat. Commun.* **9**, 812 (2018).